Lanthanide Podates with Programmed Intermolecular Interactions: Luminescence Enhancement through Association with Cyclodextrins and Unusually Large Relaxivity of the Gadolinium Self-Aggregates

Nicolas Fatin-Rouge,[†] Éva Tóth,[†] Didier Perret,[†] Robin H. Backer,[‡] André E. Merbach,[†] and Jean-Claude G. Bünzli*,[†]

Contribution from the Institute of Inorganic and Analytical Chemistry, University of Lausanne, BCH, CH-1015 Lausanne, Switzerland, and the Institute of Physical Chemistry, Swiss Federal Institute of Technology, CH-1015 Lausanne, Switzerland

Received March 28, 2000

Abstract: The synthesis of the phenyl anchored podand H_4L^1 fitted with four 3-carboxylate pyrazole arms and programmed for intermolecular interactions is reported, and its protonation constants are determined. Interaction with Ln^{3+} ions (Ln = La, Eu, Lu) in dilute aqueous solutions leads to complexes with 1:1 and 1:2 metal−ligand stoichiometry. The stability constants are in the range log β_{110} = 12.7−13.5 and log β_{120} = 22.5−23.8 (pLn values in the range 9−10). The podates display a fair sensitization of the metal-centered luminescence with an absolute quantum yield of 5% in case of Tb^{III}. The average numbers of water molecules coordinated to the Ln^{III} ion amount to 3.8 and 4.9 for the 1:1 Eu and Tb podates, respectively, as determined by lifetime measurements. The addition of β- and γ-cyclodextrins to the 1:1 podates results in a strong association with the host, mainly through the phenyl anchor (Ln = Tb, log K_{11} = 5−6 depending on the cyclodextrin) and, for the Tb complex, to a large increase in luminescence intensity at physiological pH. Self-aggregation of the podates occurs at concentration larger than 3×10^{-5} M. This process is characterized by luminescence, using a pyrene probe, light-scattering measurements, and transmission electron microscopy. The novelty of the reported systems is their ability to self-aggregate into nanometric, rigid, and spherical particles in a controlled way (mean diameter: 10, 60, and ∼300 nm), opening large perspectives for various applications. In particular, a record-high relaxivity (r_1 = 53 mM^{-1} s^{-1} at 20 MHz, T = 25 °C) is observed for the aggregates of 1:2 Gd podate, which is not modified upon addition of an equimolar quantity of Zn^{II}.

Introduction

Lanthanide(III) poly(aminocarboxylates) are widely used as luminescent probes in fluoroimmunoassays[1] and as contrast agents for magnetic resonance imaging (MRI).[2] Luminescent stains have specific requirements regarding the environment of the metal ion and the energy of the singlet and triplet states of the ligating groups.[3] Indeed, sensitization of the metal ion luminescence is usually achieved through energy transfer from the ligands since the oscillator strengths of the forbidden f−f transitions are very faint. A considerable luminescence enhancement can be obtained if the emitting ion is inserted in polymeric structures containing nonluminescent ions, e.g., Y^{III}.[4] On the other hand, the relaxivity of low molecular weight Gd^{III}-containing contrast agents is mainly limited by their fast rotational motion, and since the relaxivity of sphere-shaped molecules increases approximately linearly with molecular weight, researchers are devoting major efforts to the incorporation of gadolinium chelates in large structures such as polymers,[5] dendrimers,[6] proteins,[7] and micelles.[8] Several of these approaches are based on supramolecular chemistry[9,10] and self-organization.[8] For instance, poly-β-cyclodextrins have been used to bind Gd poly(aminocarboxylate) chelates bearing a lipophilic phenyl tail[9] and polymetallic Gd-containing edifices are self-assembled through secondary recognition involving octahedral transition metals.[10]

Developing strategies to synthesize supramolecular functional nanostructures is a major goal in modern lanthanide chemistry.[11] Association of monomers into reversible supramolecular structures can be realized by exploiting short-distance interactions through molecular recognition based upon complementary size, shape, and chemical functionalities.[12] Hydrogen bonds, aromatic π-stacking, and van der Waals interactions are valuable tools

* To whom correspondence should be addressed. E-mail: jean-claude.bunzli@icma.unil.ch.

† University of Lausanne.

‡ Swiss Federal Institute of Technology.

(1) *Bioanalytical Applications of Labeling Technologies*, 2nd ed.; Hemmilä, I., Stålberg, T., Mottram, P., Eds.; Wallac-Oy: Turku, 1995,

(2) Caravan, P.; Ellison, J. J.; McMurry, T. J.; Lauffer, R. B. *Chem. Rev.* **1999**, *99*, 2293.

(3) Bünzli, J.-C. G.; Ihringer, F.; Besançon, F. In *Calixarenes for Separations*; Lumetta, G., Rogers, R. D., Gopalan, A. C., Eds.; ACS Symposium Series; American Chemical Society, Washington, DC, 2000; Chapter 14.

(4) Latva, M.; Takalo, H.; Simberg, K.; Kankare, J. *J. Chem. Soc., Perkin Trans. 2* **1995**, 995.

(5) Desser, T.; Rubin, D.; Muller, H.; Qing, F.; Khodor, S.; Zannazzi, S.; Young, S.; Ladd, D.; Wellons, J.; Kellar, K.; Toner, J.; Snow, R. *J. Magn. Reson. Imaging* **1994**, *4*, 467.

(6) Tacke, J.; Adam, G.; Claben, H.; Muhler, A.; Prescher, A.; Gunther, R. W. *J. Magn. Reson. Imaging* **1997**, *7*, 678.

(7) Lauffer, R. B.; Brady, T. J. *J. Magn. Reson. Imaging* **1985**, *3*, 11.

(8) André, J. P.; Tóth, E.; Fischer, H.; Seelig, A.; Maecke, H. R.; Merbach, A. E. *Chem. Eur. J.* **1999**, *5*, 2977.

(9) Aime, S.; Botta, M.; Frullano, L.; Geninatti Crich, S.; Giovenzana, G. B.; Pagliarin, R.; Palmisano, G.; Sisti M. *Chem. Eur. J.* **1999**, *5*, 1253.

(10) Jacques, V.; Hermann, M.; Humblet, V.; Sauvage, C.; Desreux, J. F. *Coord. Chem. Rev.* **1999**, *185*, 451.

(11) Piguet, C.; Bünzli, J.-C. G. *Chem. Soc. Rev.* **1999**, *28*, 347.

10.1021/ja001089b CCC: $19.00
Published on Web 10/21/2000

Chart 1

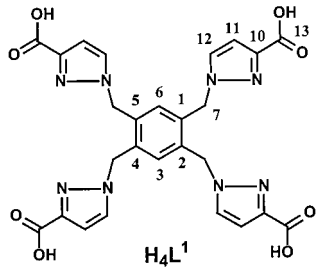

for the supramolecular chemist, and since the associated enthalpies are weak, the design of the monomers must be focused on maximizing the reaction's entropy.[13] That is, the monomers should be rigid enough to ensure good intermolecular contact between interacting surfaces, and release of water upon association of hydrophobic regions of the aggregating molecules is needed to overcome the unfavorable loss of translational entropy of the monomers.

Pursuing our efforts to design lanthanide-containing chelating systems with potential applications as both luminescent stains and contrast agents[14] and taking into account the advantage of large nanometric over molecular systems, we present here the design of chelates able to associate through noncovalent intermolecular interactions with a potential carrier such as a cyclodextrin and/or to self-aggregate into larger entities. We have turned our attention to podands built from a benzene anchor and pyrazole-containing arms. The benzene ring is essentially meant to protect the metal ion from outside interaction while the pyrazole groups are known to provide a good antenna effect.[15−17] We have modified the poly(pyrazole) ligands developed by Hartsorn and Steel[18,19] for Ru^{II} complexation by adding carboxylate groups at the 3-position of the pyrazole rings because these groups are hydrophilic and they complex strongly trivalent Ln ions. In this paper, we present the synthesis of ligand H_4L^1, 1,2,4,5-tetrakis(pyrazol-1-ylmethyl-3-carboxylic acid)-benzene (Chart 1), a study of its complexation ability with trivalent Ln ions (Ln = La, Eu, Lu) and of the luminescent properties of the Eu and Tb podates alone or as host−guest complexes with cyclodextrins (Tb). In addition, the formation of nanometric self-aggregates is investigated by several experimental techniques and its consequence on the relaxivity of the Gd complexes is presented.

Experimental Section

Starting Materials and General Procedures. Solvents and chemicals (Fluka AG) were of analytical grade and used without further purification except tetrahydrofuran and dry ethanol, which were distilled from CaH_2 and CaO, respectively. Solutions were prepared just before use with freshly boiled, doubly distilled water saturated with N_2. Stock solutions of $LnX_3 \cdot nH_2O$ (X = ClO_4, Cl, CF_3SO_3, AcO) were prepared from lanthanide oxides (99.99%, Glucydur) and the corresponding acid. They were systematically acidified with HCl to pH ∼4 before titration to avoid $Ln(OH)_3$ precipitation. The concentrations were determined by complexometric titrations using a standardized Na_2H_2EDTA solution in urotropine buffered medium and xylene orange as indicator. The concentrations of stock solutions of cyclodextrins (CDs) were calculated from the optical rotation (deg) of sodium light at 25.0 °C: permethylated β-CD (βpm-CD) = 160 ± 5, β-CD = 162.5 ± 0.5, and γ-CD = 177.5 ± 0.5.[20] Elemental analyses were performed by Dr. Eder, Microchemical Laboratory, University of Geneva.

1D and 2D NMR data were collected on DPX-400 or AM-360 Bruker spectrometers. ^1H NMR spectra were recorded in D_2O or CH_3OD and ^{13}C spectra in D_2O with acetonitrile as external reference.[21] Assignment of ^1H and ^{13}C spectra was based on ^1H coupling and 2D $^1H-^{13}C$ correlation spectra. Assignment of the signals for C_{11} and C_{12} was made using computation of electric charge density (AM1 package, Hyperquem[22]). The mass spectra were recorded in electrospray ionization mode on a VG BioQ quadrupole mass spectrometer (T_{matrix} = 100 °C). The instrument was calibrated using the horse myoglobin standard. The analyses were conducted in both positive and negative modes. The ion spray voltage was 4,6 kV, and CID voltage was 20−40 V. Assignment of the species was based on the isotopic distribution of the peaks. Electronic UV−visible spectra were recorded on a Perkin-Elmer Lambda 7 spectrometer. Infrared spectra were measured on a FT-IR Mattson Alpha Centauri spectrometer (4000−400 cm^{-1}, KBr pellets).

Syntheses. 3-Carboxylic Acid−Pyrazole. 3-Methylpyrazole (9.8 mL, 0.117 mol) was dissolved in 450 mL of water. To this solution, 40.9 g of aqueous $KMnO_4$ (2.2 equi, 0.259 mol) was added slowly at room temperature and the mixture was refluxed 4 h. The solution was cooled, filtered, and evaporated to a small volume. Recrystallization was performed in water at pH ∼2. After 1 h at 4 °C, white crystals (yield 100%) were collected and washed with cold acidic water: R_f = 0.83 ($CHCl_3/CH_3OH$/25% aqueous NH_3, 2/4/1); ^1H NMR (D_2O) δ 7.78 (d, J = 2.4 Hz, 1H) and 6.89 (d, J = 2.4 Hz, 1H).

3-Ethyl Ester−Pyrazole. The ester was made under nitrogen flow by refluxing for 5 h 1.02 g of the dried acid (9.1×10^{-3} mol) in 20 mL of absolute ethanol and 1.5 mL of concentrated sulfuric acid. The solvent was then evaporated, and a yellow oil was obtained. Water (50 mL) was added to dissolve the substance, and the solution was neutralized with $NaHCO_3$. The product was extracted with ethyl acetate, the solvent was partially evaporated, and addition of a few milliliters of petroleum ether initiated crystallization of a white material (85% yield): R_f = 0.53 (CH_2Cl_2/CH_3OH, 95/5), ^1H NMR ($CDCl_3$) δ 7.62 (d, J = 2.4 Hz, 1H), 6.87 (d, J = 2.4 Hz, 1H), 4.42 (q, J = 7.2 Hz, 2H), 1.40 (t, J = 7.2 Hz, 3H).

1,2,4,5-Tetrakis(3-ethyl ester pyrazole-1-yl-methyl)benzene. 3-Ethyl ester−pyrazole (1.40 g, 0.01 mol) and sodium (0.276 g, 0.012 mol) were reacted in dry ethanol. After dissolution, tetrakis(bromomethyl)-benzene ($^1/_4$ equiv) in 30 mL of dry THF was added dropwise under reflux; the mixture was further refluxed 1 h and evaporated to dryness. Yield: 50%. ^1H NMR ($(CD_3)_2CO$) δ 7.78 (d, J = 2.4 Hz, 4H), 6.84 (d, J = 2.4 Hz, 4H), 6.72 (s, 2H), 5.59 (s, 8H), 4.30 (q, J = 7.2 Hz, 8H), 1.32 (t, J = 7.2 Hz, 12H); ESI-MS, $[M + Na]^+$ 709.8 (calcd 709.7), $[M + K]^+$ 725.9 (calcd 725.8); IR (KBr, cm^{-1}) 1720 (C═O) , 1480 (C═C) , 1378 (C−N), 2895 (C−H).

Preparation of L^1. The tetraester was hydrolyzed overnight with KOH (1.2 equiv) in 40 mL of water at 50 °C. The yellow solution was washed with ether (4 × 50 mL), and the aqueous phase was transferred into centrifugation tubes, adjusted to pH ∼2 (concentrated HCl), and cooled to 0 °C, and the precipitate was collected by centrifugation. This procedure was repeated several times. The isolated ligand was washed successively with cold water (100 mL), ether (80 mL), methylene dichloride (50 mL), and acetone (50 mL). Yield: 47%. R_f = 0.77 ($CHCl_3/CH_3OH$/25% aqueous NH_3, 4/9/1); ^1H NMR (D_2O, 20° C) δ 5.4 (H^1), 6.3 (H^3, H^6), 6.6 (H^{11}), 7.4 (H^{12}); ^{13}C NMR (D_2O, 20 °C) δ 52.3 (C^7), 107.8 (C^3, C^6), 128.2 (C^{11}), 132.4 (C^{12}), 134.8 ($C^{1,2}$,

(12) Lehn, J. M. *Supramolecular Chemistry, Concepts and Perspectives*; VCH: Weinheim, 1995.
(13) Whitesides, G. M.; Mathias, J. P.; Seto C. T. *Science* **1991**, *254*, 1312.
(14) Zucchi, G.; Scopelliti, R.; Pittet, P.-A.; Bünzli, J.-C. G.; Rogers, R. D. *J. Chem. Soc., Dalton Trans.* **1999**, 931.
(15) Reeves, Z.; Mann, K.; Jeffery, J.; McCleverty, J. *J. Chem. Soc., Dalton Trans.* **1999**, 349.
(16) Lawrence, R.; Jones, C.; Kresinski, R. *Inorg. Chim. Acta* **1999**, *285*, 283.
(17) Sanada, T.; Suzuki, T.; Yoshida, T.; Kaizaki, S. *Inorg. Chem.* **1998**, *37*, 4712.
(18) Hartsorn, C.; Steel, P. *Aust. J. Chem.* **1995**, *48*, 1587.
(19) Hartsorn, C.; Steel, P. *Angew. Chem., Int. Ed. Engl.* **1996**, *35*, 2655.
(20) French, D.; Levine, M.; Pazur, J.; Norberg, E. *J. Am. Chem. Soc.* **1949**, *71*, 353.
(21) Gottieb, H.; Kotlyar, V.; Nudelman, A. *J. Org. Chem.* **1997**, *62*, 7513.
(22) Dewar, M. J. S.; Zoebisch, E. V.; Healy, E. F.; Stewart J. J. P. *J. Am. Chem. Soc.* **1985**, *107*, 3902.

$C^{4,5}$), 149.1 (C^{10}), 169.7 (C^{13}); ESI-MS. $[M + Na]^+$ 597.8 (calcd 597.5), $[M + K]^+$ 613.9 (calcd 613.6); IR (KBr, cm^{-1}) 3407 br (aryl CO*OH*), 2533 br (overtone, aryl CO*OH*), 1712 (C═O(OH)), 1509 (C═C), 1379 (C−N), 1060 (C−O). Elemental Anal. Found: C, 53.60; H, 4.68; N, 17.49. Calcd for $C_{26}H_{22}N_8O_8\cdot(CH_3)_2CO\cdot H_2O$: C, 53.52; H, 4.65; N, 17.23. Acetone was indeed found in the ^1H NMR spectrum and integration accounted for six protons.

Preparation of $(H_3O)[LnL^1]\cdot$solv Podates (Ln = La, Eu, Gd, Tb, Lu). Freshly titrated $LnCl_3.nH_2O$ solutions (∼0.025 M, ∼1,2 mL, ∼0.03 mmol) were added slowly, at room temperature, to an aqueous solution of K_3HL^1 (∼25 mg, ∼0.03 mmol, 4 mL, pH 7.1 (adjusted with HCl)). When turbidity appeared, the pH was adjusted to 7.1 with 0.1 M KOH; the solution was then transferred into a centrifugation flask, cooled at 4 °C for 2 h, and centrifuged. The collected material was washed with methanol (4 mL) to remove the unreacted ligand and sonicated. The precipitation procedure was repeated three times. The solid was dried, washed with 20 mL of acetone on a sinter filter, and further dried for 1.5 days at 65 °C and 0.01 Torr. Yield: ∼60%.

$(H_3O)[LaL^1]$: IR (KBr, cm^{-1}) 3411 br (OH), 1580 and 1371 (ν_{as}, ν_s COO), 1514, 1485, 1420, 1299, 1192, 1060, 770. Elemental Anal. Found: C, 41.66; H, 4.03; N, 14.20. Calcd for $(H_3O)[LaL^1]\cdot 2CH_3OH\cdot H_2O$, $C_{28}H_{31}N_8O_{12}La$: C, 41.48; H, 3.86; N, 13.83.

$(H_3O)[EuL^1]$: IR (KBr, cm^{-1}) 3415 br (OH), 1590 and 1371 (ν_{as}, ν_s COO), 1519, 1486, 1420, 1299, 1192, 1057, 770. Elemental Anal. Found: C, 41.08; H, 3.57; N, 14.03. Calcd for $(H_3O)[EuL^1]\cdot CH_3OH\cdot 2H_2O$, $C_{27}H_{29}N_8O_{12}Eu$: C, 40.00; H, 3.61; N, 13.83.

$(H_3O)[GdL^1]$: IR (KBr, cm^{-1}) 3411 br (OH), 1590 and 1371 (ν_{as}, ν_s COO), 1519, 1486, 1420, 1299, 1192, 1058, 770 cm^{-1}. Elemental Anal. Found: C, 40.04; H, 3.42; N, 13.68. Calcd for $(H_3O)[GdL^1]\cdot 3H_2O$, $C_{26}H_{27}N_8O_{12}Eu$: C, 38.95; H, 3.40; N, 13.98.

$(H_3O)[TbL^1]$: IR (KBr, cm^{-1}) 3422 br (OH), 1601 and 1371 (ν_{as}, ν_s COO)IR ν_{max}, 1520, 1487, 1420, 1300, 1199, 1061, 773. Elemental Anal. Found: C, 40.95; H, 3.72; N, 14.30. Calcd for $(H_3O)[TbL^1]\cdot 2CH_3OH$, $C_{28}H_{29}N_8O_{11}Tb$: C, 41.37; H, 3.60; N, 13.79.

$(H_3O)[LuL^1]$: IR (KBr, cm^{-1}) 3430 br (OH), 1627 and 1369 (ν_{as}, ν_s COO), 1507, 1486, 1421, 1295, 1192, 1065, 768 cm^{-1}. Elemental Anal. Found: C, 38.38; H, 3.30; N, 13.30. Calcd for $(H_3O)[LuL^1]\cdot 3H_2O$, $C_{26}H_{27}N_8O_{12}Lu$: C, 38.14; H, 3.33; N, 13.69.

Preparation of $K_5[Ln(L^1)_2]\cdot$solv (Ln = La, Eu, Tb, Lu) and $(H_3O)_5[Gd(L^1)_2]\cdot$solv. Freshly titrated $LnCl_3\cdot nH_2O$ solutions (∼0.025 M, ∼0.6 mL, ∼0.015 mmol) were added slowly at room temperature to an aqueous solution of K_3HL^1 (∼25 mg, ∼0.03 mmol, 4 mL, pH 9.1) or H_4L^1 (15.1 mg, 2.61×10^{-5} mol). The pH was adjusted to 8.0 with 0.1 M KOH (7.2 for Gd); the solution was partially evaporated with N_2 and centrifuged. For Gd, the solution was left 1 day at room temperature, transferred in a centrifugation flask, methanol (∼1 mL) was added, and precipitation of the complex was started with a few drops of ether; a turbidity appeared and the solution was cooled 2 h at 4 °C and centrifuged. The collected materials were washed on a sinter filter with acetone (∼100 mL) and then methanol (∼10 mL). The solids were dried for 1.5 day at 65 °C and 0.01 Torr. Yield: ∼70%.

$K_5[La(L^1)_2]$: IR (KBr, cm^{-1}) 3418 br (OH), 1592 and 1371 (ν_{as}, ν_s COO), 1514, 1482, 1414, 1304, 1192, 1058, 812, 770 cm^{-1}. Elemental Anal. Found: C, 38.72; H, 3.55; N, 13.44. Calcd for K_5 $[La(L^1)_2]\cdot 2CH_3OH\cdot 7H_2O$, $C_{54}H_{58}N_{16}O_{25}K_5La$: C, 38.94; H, 3.51; N, 13.46.

$K_5[Eu(L^1)_2]$: IR (KBr, cm^{-1}) 3420 br (OH), 1594 and 1371 (ν_{as}, ν_s COO), 1514, 1478, 1412, 1302, 1192, 1054, 810, 770. Elemental Anal. Found: C, 37.25; H, 3.31; N, 13.02. Calcd for K_5 $[Eu(L^1)_2]\cdot 10H_2O$, $C_{52}H_{56}N_{16}O_{26}K_5Eu$: C, 37.41; H, 3.38; N, 13.43.

$K_5[Tb(L^1)_2]$: IR (KBr, cm^{-1}) 3438 br (OH), 1622 and 1371 (ν_{as}, ν_s COO), 1505, 1421, 1299, 1201, 829, 770. Elemental Anal. Found: C, 37.49; H, 3.38; N, 13.00. Calcd for K_5 $[Tb(L^1)_2]\cdot 10H_2O$, $C_{52}H_{56}N_{16}O_{26}K_5Tb$: C, 37.27; H, 3.37; N, 13.38.

$K_5[Lu(L^1)_2]$: IR (KBr, cm^{-1}) 3438 br (OH), 1624 and 1367 (ν_{as}, ν_s COO), 1569, 1506, 1421, 1299, 1201, 1190, 1070, 836, 772. Elemental Anal. Found: C, 35.66; H, 3.34; N, 12.58. Calcd for $K_6[Lu(L^1)_2(OH)]\cdot 10H_2O$, $C_{52}H_{57}N_{16}O_{27}K_6Lu$: C, 35.74; H, 3.29; N, 12.83.

$(H_3O)_5[Gd(L^1)_2]$; IR (KBr, cm^{-1}) 3422 br (OH), 1599 and 1371 (ν_{as}, ν_s COO), 1521, 1487, 1421, 1299, 1201, 829, 770. Elemental Anal. Found: C, 44.02; H, 4.22; N, 14.34. Calcd for $(H_3O)_5[Gd(L^1)_2]\cdot(CH_3)_2CO\cdot 4H_2O$, $C_{55}H_{65}N_{16}O_{26}Gd$: C, 43.33; H, 4.30; N, 14.71.

Solutions for Mass Spectrometry Analysis (ESI-MS). The Eu complexes were prepared in pure methanol, mixing $Eu(CF_3SO_3)_3$ and the ligand in stoichiometric ratios at 10^{-4} M. $[Eu(L^1\text{-}H)]^{2+}$. $m/z = 364.1$ (calcd 364.04); $[Eu(L^1\text{-}4H)_2(H_2O)]^{5-}$, $m/z = 262.7$ (calcd 262.8); $[Eu(L^1 - 4H)_2(MeOH)]^{5-}$, $m/z = 264.9$ (calcd 265.0).

Physicochemical Characterization of the Monomeric Podates. Potentiometric Titrations. Titrations of H_4L^1 or Ln^{3+} alone or 1:1 mixtures ($[L^1]_t = [Ln]_t = 1.0 \times 10^{-3}$ M) were carried out using 5-mL sample solutions in a thermostated (20.0 ± 0.1 °C) glass-jacketed vessel in an atmosphere of Ar. The ionic strength was fixed with KCl (μ = 0.1 M). Reactants were mixed and acidified to pH ∼2 (HCl) at least 30 min before titration. Titrations were carried out with an automatic Metrohm Titrino 736 GP potentiometer (resolution 0.1 mV, accuracy 0.2 mV) using a constant-volume addition (0.05 mL) program and linked to an IBM PS/2 computer. An automatic buret (Metrohm 6.3013.210) 10 mL, accuracy 0.03 mL, was used along with a Metrohm 6.0238.000 glass electrode. The standard base (KOH 0.010 M) or acid (HCl 0.010 M) (μ = 0.1 M, KCl) was added through a capillary tip inside the solution attached to the automatic buret. The data (130 points per curve, drift <1 mV/mn) were mathematically treated by the program SUPERQUAD[23] using a Marquardt algorithm while the distribution of species was calculated with the program Haltafall.[24] Calibration of the pH-meter and the electrode system was performed prior to each measurement using a standardized HCl solution (μ = 0.1 M, KCl) at 20.0 °C. The ion product of water ($pK_w = 13.98$) and electrode potential were refined using the program Scientist by Micromath (version 2.0). The stepwise protonation constants of the deprotonated ligand $[L^1]^{4-}$ are defined as $\beta_i = [H_iL^1]^{(4-i)-}/[H_{i-1}L^1]^{(5-i)-}\cdot[H^+]^i$, and the overall equilibrium constants describing all metal−ligand-proton species, $M_iL_jH_k$, are equal to $\beta_{ijk} = [M_iL_jH_k]/[M]^i[L]^j[H^+]^k$.

Spectrophotometric Titrations. Electronic spectra were recorded with a Perkin-Elmer Lamdba 7 spectrophotometer at 20.0 °C (210−500 nm, 100 nm mn^{-1} scan speed, spectral width 1 nm) using 1-cm Suprasil quartz cells. Titrations of L^1 (1.9×10^{-5} M, 15.0 mL, $[HCl]_{tit}$ = 0.050 M, μ = 0.1 (KCl) or 3.5×10^{-5} M, 19.7 mL, $[LaCl_3]_{tit} = 1.09 \times 10^{-3}$ M, pH 7.0 (Pipes buffer 10^{-3} M), μ = 0.1 M (KCl)) were performed in a thermostated (20.0 ± 0.1 °C) glass-jacketed vessel in an atmosphere of Ar. Aliquots of titrant were added using a Socorex micropipet. The pH values of the titrated solutions were controlled continuously. Under these conditions, equilibrium was attained within 10 min, as checked by kinetic measurements. After this delay, 3 mL of solution was transferred into the quartz cell with a Teflon syringe. No evidence of aggregation, e.g., turbidity, was detected along the titration. The stability constants (apparent for La^{3+} complexation or true for H^+ complexation) were computed using the Specfit program.[25] Differences between the measured and the computed absorbances were less than 0.004 at any wavelength.

NMR Titrations. Ligand, 10^{-3}−10^{-2} M solutions, was prepared in 2 mL of D_2O. Sample solutions with different pD values were prepared by adding dilute KOD/D_2O or dilute D_2SO_4/D_2O (Fluka, puriss). The pH values of the solutions were determined with a Metrohm Titrino 736 GP potentiometer equipped with a calibrated Metrohm 6.0234.100 glass electrode. Measurements of the potential of a borate buffer solution either in H_2O or in D_2O allowed us to convert to pD values by the equation, $pD = pH_{meas} + 0.17$. Ionic strength was not adjusted.

Luminescence Titrations. $[LnL^1{}_i]^{(4i-3)-}$ (5×10^{-6} M; V_0 = 10 mL; Ln = Tb, Gd; i = 1, pH 7.2; i = 2, pH 9.4) were titrated with 0.01 M aqueous solutions of βpm-, β-, and γ-CDs using the same procedure as described for potentiometric and spectrophotometric titrations. Equilibrium was reached within 10 min delay as checked by kinetic measurements. After this delay, 3 mL of solution was transferred into a quartz cell and degassed for 5 min with Ar. Absorbance at the excitation wavelength was measured (A < 0.05), and emission (λ_{exc} = 260 nm) and excitation spectra were collected. Each titration was made twice. Ionic strength was not adjusted.

(23) Gans, P.; Sabatini, A.; Vacca, A. *J. Chem. Soc., Dalton Trans.* **1985**, 1195.

(24) Ingri, N.; Kakolowicz, W.; Sillen, L. G.; Warnqvist, B. *Talanta* **1967**, *14*, 1261−1286.

(25) Gampp, H.; Maeder, M.; Meyer, C.; Zuberbühler, A. *Talanta* **1986**, *33*, 943.

Luminescence Measurements. Low-resolution luminescence measurements (spectra and lifetimes) were recorded on a Perkin-Elmer LS-50B spectrofluorometer. Phosphorescence lifetimes (τ) were measured with the instrument in time-resolved mode, on frozen ethanol solutions put into a quartz capillary or a 1-cm Suprasil cell at room temperature. They are the average of at least three independent measurements which were made by monitoring the decay at the maximums of the emission spectra after a 0.03−0.04-ms delay time. The signals were usually analyzed as single-exponential decays using the program FLDM (Perkin-Elmer). Solutions of $[Ln(L^1)_i]^{(4i-3)-}$ were prepared in water at pH 7.0, using stock solutions of H_4L^1 (2.0×10^{-3} M) and $Ln(ClO_4)_3$ (Ln = La, Eu, Gd, Tb, Lu) ($\sim 4.5 \times 10^{-3}$ M). Frozen solutions in ethanol $(0.5-1) \times 10^{-5}$ M were made using dried solutions of complexes prepared previously in water and then dissolved in ethanol (fluorescence quality). Quantum yields of $[L^1]^{4-}$ (5×10^{-6} M, pH 13.5) and $[Ln(L^1)_i]^{(4i-3)-}$ (Ln = La, Gd, Lu, $(0.5-1) \times 10^{-5}$ M in H_2O, pH 7) were determined in degassed water relative to quinine sulfate in 0.05 M aqueous H_2SO_4 (absolute quantum yield 0.546[26]); estimated error, 10%. Metal-centered luminescence of $[Ln(L^1)_i]^{(4i-3)-}$ complexes (Ln = Eu, Tb; $(0.5-1) \times 10^{-5}$ M in H_2O, pH 7) was determined relative to degassed solutions of $[Eu(terpy)_3](ClO_4)_3$ or $[Tb(terpy)_3](ClO_4)_3$ 10^{-3} M in acetonitrile (terpy = 2,2′:6′,2″-terpyridine, absolute quantum yields 1.3.[27] and 4.8%,[28] respectively); the estimated error is 30%. The number of coordinated water molecules (q) for the Eu podates was calculated from $q = n(\tau^{-1}_H - \tau^{-1}_D)$, where τ_H and τ_D are the lifetimes in H_2O and D_2O, respectively, and $n = 1.05$.[29]

Physicochemical Characterization of the Self-aggregated Particles. Determination of Critical Aggregation Concentrations (cac). A stock solution of $[L^1]_t = 3.6 \times 10^{-3}$ M and $[GdCl_3]_t = 1.5 \times 10^{-3}$ M at pH 9.2 was added to known volumes of water at the same pH. The solutions were allowed to equilibrate at room temperature for 20 min, and the pH was adjusted with 0.1 M KOH and HCl solutions. For fluorescence measurements, the initial volume of water was saturated with pyrene ($\sim 10^{-7}$ M) and the samples were degassed with argon. The emission spectra of pyrene were recorded from 350 to 500 nm ($\lambda_{exc} = 337$ nm, excitation and emission band-path 5 nm, scan rate 50 nm min^{-1}). Two scans were accumulated for each run and were corrected before the ratio of intensities of the first (363 nm) and third (382 nm) vibrational peaks, I_1/I_3, was calculated. Dynamic light-scattering measurements were performed at 22.0 ± 0.1 °C in a toluene bath at a scattering angle of 90°, using a He−Ne laser light-scattering instrument operating at 632.8 nm. The intensity of the light scattered by toluene was used as reference. Diffusion coefficients of particles in H_2O were determined from an exponential fit to the correlation curve. Hydrodynamic radii were calculated from measured diffusion coefficients by means of the Stokes−Einstein equation.

Transmission Electron Microscopy (TEM) of the Gd Self-Aggregates. Collodion-covered (<10 nm), carbon-coated (<10 nm) TEM gold grids were used as specimen holders. Collection of particles was achieved in two ways: (a) by ultracentrifugation[30] of a 1.1×10^{-4} M solution of the 1:2 Gd^{III} complex at pH 9.2. After centrifugation, the supernatant liquid was carefully withdrawn and the grids were immediately rinsed with a drop of ultrapure water to avoid formation of KCl microcrystals. (b) By depositing 2 μL of solution of the 1:2 (1.1×10^{-4} M, pH 9.2) or 1:1 (4×10^{-5} M, pH 7.0) Gd podate on the gold grid, washed with a drop of water. The grids were observed in a Philips CM 12 electron microscope using a 40-μm aperture at an acceleration of 80 keV. Spectral analysis was made by energy dispersion spectroscopy (EDS) with an EDAX DX-4 probe. The aggregation regime of $\{Gd(L^1)_2{}^{5-}\}_n$ into particles was assessed by image-fractal analysis. Electron micrographs were digitized (2000 lpi, 8-bits depth; intensity and contrast kept constant), and the morphometric characteristics of the particles and aggregates were determined on gray level images (AnalySIS, Soft Imaging Systems). To ensure consistent results, the scanned areas (0.64 μm^2) were divided into subframes (0.04−0.16 μm^2) and the background (collodion/carbon film) was subtracted from each individual entity. The average net gray value of the objects was converted into mean particle thickness by calibration with 15−30-nm spherical colloids. By this method, the maximum local thickness <5% of the analyzed entities was underestimated (some region of the entity obviously fell outside the maximum black level). The mechanism of aggregation was determined by fitting the volume $(V_{calc})_{agg}$ of the entities as a function of $((R_g)_{agg}/(a)_{unit})^f$ with a least-squares Levenberg−Marquardt algorithm (Origin; Microcal), where $(R_g)_{agg}$ is the radius of gyration of the entity, $(a)_{unit}$ is the radius of its constituting elementary colloids, and f is the fractal dimension.[31,32] The error on the final result was estimated by maximizing the inaccuracies at each step of the measurement.

Electrophoretic Mobility (μ_e). The value of μ_e and the zeta-potential (ζ) for the $\{Gd(L^1)_2\}_n{}^{5n-}$ self-aggregated particles were determined using a Zetasizer IV (Malvern Instruments) electrophoretic light-scattering apparatus, previously calibrated with anionic latexes. Measurements were made at 20.0 ± 0.1 °C with an aqueous solution of complex ($[L^1]_t = 1.1 \times 10^{-2}$ M and $[GdCl_3]_t = 5 \times 10^{-3}$ M at pH 7.4) sufficient to produce a photon counting rate of at least 2×10^6 counts/s; μ_e and ζ data reported are averages of five independent analyses. Calculation of ζ from measured μ_e was obtained from the built-in software supplied with the instrument. The model used in the calculation was the Smoluchowski limit ($\kappa a \gg 1$) for which the general relationship between ζ and μ_e reduces to the simple expression: $\mu_e = \epsilon\zeta/\eta$, where ϵ is the dielectric constant of the medium, η is the dynamic viscosity, κ the inverse double-layer thickness and a is the hydrated particle radius. The surface charge density (σ_0) of the aggregates was evaluated from the dimension-less surface potential (Ψ_0), the potential Ψ at the distance x from the surface and ζ, according to the following equations:[33]

$$\sigma_0 = 2\sqrt{2\epsilon n_i k_B T}\,\sin(\Psi_0/2)$$

$$\Psi_0 = 4\arctan\left(\frac{e^{(\Psi/2)-1}}{(1+e^{\Psi/2})e^{-\kappa x}}\right), \quad \text{with} \quad \Psi = \frac{\zeta e z}{k_B T}$$

$$\kappa^{-1} = \sqrt{\epsilon k_B T/e^2 \sum_i z_i n_i}$$

where ϵ is the dielectric constant, n_i the number of ions per cubic meter, z_i their charge, k_B Boltzman's constant, and T the absolute temperature.

Proton Relaxivity Measurements. The nuclear magnetic relaxation dispersion (NMRD) profiles have been measured at 5, 25. and 75 °C for $[Gd(L^1_2)]^{5-}$ (1.5×10^{-3} M, pH 7.3) on a Stelar Spinmaster FFC fast-field cycling NMR relaxometer and on a Bruker electromagnet, covering a continuum of magnetic fields from 7×10^{-4} to 1.41 T (corresponding to a proton Larmor frequency range 0.03−60 MHz). For $[GdL^1]^-$ (4×10^{-5} M; pH 7.3), the water relaxivity has been measured at 25 °C and 20 MHz only. The transverse electron spin relaxation rate has been obtained from the measured peak-to-peak EPR line widths of the derivative EPR spectrum, recorded on a Bruker ESP 300E spectrometer (X-band; 0.34 T).

Results and Discussion

Protonation Constants of $[L^1]^{4-}$. Protonation constants were determined by spectrophotometry (Figure F1, Supporting Information) and were checked with pH potentiometry. The first protonation constant was easily obtained because substantial changes occur between pH 8 and 13 in the carboxylate

(26) Meech, S. R.; Philips, D. J. *J. Photochem.* **1983**, *23*, 193.
(27) Martin, N.; Bünzli, J.-C. G.; McKee, V.; Piguet, C.; Hopfgartner, G. *Inorg. Chem.* **1998**, *37*, 577.
(28) Charbonnière, L. J.; Balsiger, C.; Schenk, K. L.; Bünzli, J. C. B. *J. Chem. Soc., Dalton Trans.* **1998**, 505.
(29) *Lanthanide Probes in Life, Chemical and Earth Sciences*; Bünzli, J. C. G., Choppin G. R., Eds.; Elsevier Science Publ. B. V.: Amsterdam, 1989.
(30) Lienemann, C. P.; Heissenberger, A.; Leppard, G. G.; Perret, D. *Aquat. Microb. Ecol.* **1998**, *14*, 205.
(31) *The Fractal Geometry of Nature*; Mandelbrot, B. B., Ed.; Freeman: San Francisco, 1982.
(32) Lin, M. Y.; Lindsay, H. M.; Weitz, D. A.; Ball, R. C.; Klein, R.; Meakin, P. *Nature* **1989**, *339*, 360.
(33) James, A. M. *Electrophoresis of Particles in Suspensions*; Plenum Press: New York, 1979; Vol. 11, p 121ff.

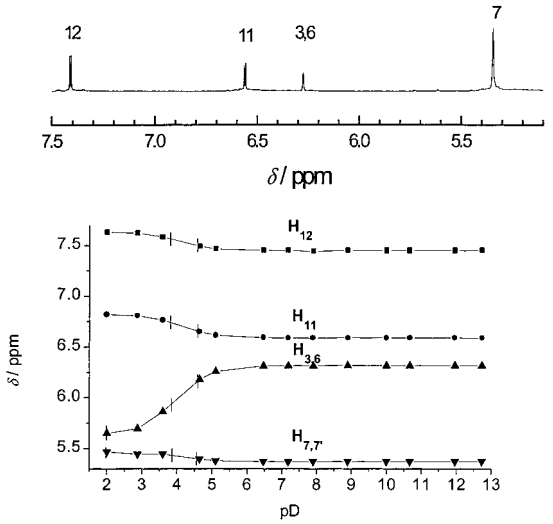

Figure 1. ^{1}H NMR spectrum of $[L^1]^{4-}$ at pD = 12.9 and variations of δ vs pD; T = 20 °C.

chromophore zone of the UV-spectra around 210 nm. Two other bands were monitored during the titration, one at 230 nm ($\epsilon \sim$ 30 000 $M^{-1}cm^{-1}$), assigned to a $\pi \rightarrow \pi^*$ transition in the pyrazole chromophore,[15] and the other at 305 nm ($\epsilon \approx$ 3300 $M^{-1}cm^{-1}$), attributed to a n $\rightarrow \pi^*$ transition in view of its low intensity. The extracted pK_a values amount to 2.0(3), 3.2(2), 4.6(1), 12.3(1) (μ = 0.1 M, KCl; 20 °C). The titration was also followed by ^{1}H NMR to get more insight into the protonation mechanism (Figure 1). No variation in chemical shifts is detected for the first proton association while substantial variations (up to 0.5 ppm) occur for phenyl protons upon the second and third protonation processes. Interestingly, both the ^{1}H and ^{13}C NMR spectra display only one set of signals during the titration, somewhat broadened in acidic media, and reflecting symmetric structures and/or the presence of fast equilibria between differently protonated species. For methylene protons directly attached to carboxylate groups, a 0.2 ppm shift is usually expected while protonation of linear aminocarboxylates leads to a chemical shift 5-fold larger when the nitrogen atom is protonated.[34] In the case of $(L^1)^{4-}$, the nearest protons are located far from the carboxylate groups. Comparing the pK_a values obtained with those of 1-methylpyrazole (pK_a = 3.6[35]), benzoic acid (pK_a = 4.2), pyridine (p$K_a \sim$ 5.4), and dipicolinic acid (pK_{a1} = 1.4 and pK_{a2} = 5.3) allows us to draw the following conclusions. Since spectrophotometric data indicate that the first protonation occurs on carboxylate groups, the unexpectedly large binding constant obtained for this first proton association (pK_{a4} = 12.33) can only be explained by invoking synergetic interactions in the ligand involving more than one arm in the proton binding. Moreover, the pK_a values expected for pyrazole nitrogen and carboxylate functions being on the same order of magnitude and large ^{1}H NMR chemicals shifts being associated with the second and third protonation, we assume that nitrogen atoms are involved in these protonation steps. The close proximity of the pyrazole and carboxylic functions on each arm probably induces a fast proton exchange between these two functions (dentate effect), as observed in bipyridyl.[36]

Interaction of H_iL^1 with Trivalent Ln Ions in Dilute Solution. The stability constants of the complexes formed between Ln^{3+} ions (Ln = La, Eu, Lu) and H_iL^1 have been determined by potentiometric titration of 1:1 ligand−metal

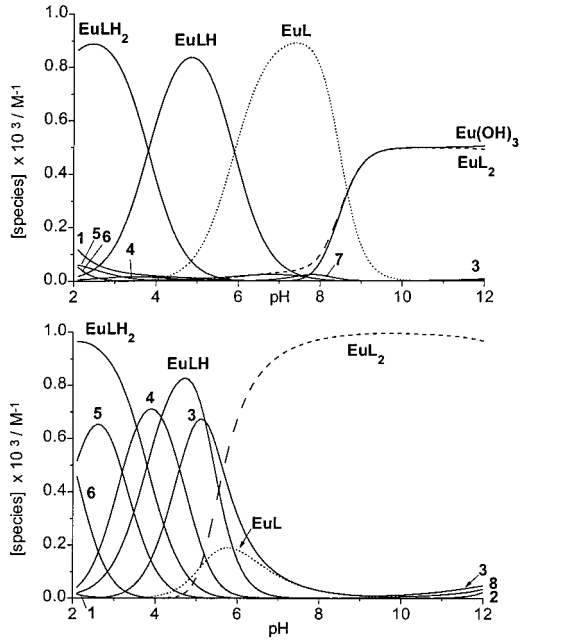

Figure 2. Computed distribution curves for the Eu/H_4L^1 system: (- - -) $[EuL^1]^-$; (— —) $[Eu(L^1)_2]^{5-}$; **(1)** Eu^{III}_{aq}; **(2)** $\{L^1\}^{4-}$; **(3)** $(HL^1)^{3-}$; **(4)** $(H_2L^1)^{2-}$; **(5)** $(H_3L^1)^-$; **(6)** H_4L^1; **(7)** $EuOH^{2+}$; **(8)** $Eu(OH)_3$. Top: $[L^1]_t = [Eu^{III}]_t = 1.0 \times 10^{-3}$ M. Bottom: $[L^1]_t = 2[Eu^{III}]_t = 2.0 \times 10^{-3}$ M. T = 20.0 °C; μ = 0.1 M (KCl).

Table 1. Stability Constants log β_{ijk} ($\pm 2\sigma$) Obtained for Complexes $Ln_iL_jH_k$ from pH Potentiometry. $[L^1]_t = [LnCl_3]_t = 1.0 \times 10^{-3}$ M; μ = 0.1 M (KCl); T = 20.0° C

i	j	k	La^{3+}	Eu^{3+}	Lu^{3+}
1	0	−1	−7.90(4)	−7.47(4)	−7.35(5)
1	0	−3	−24.92(4)	−22.96(4)	−21.78(4)
1	1	0	12.7(2)	13.4(2)	12.8(2)
1	1	1	18.5(2)	19.3(2)	18.9(2)
1	1	2	22.4(2)	23.1(2)	22.7(2)
1	2	0	23.2(2)	23.8(2)	22.5(2)

mixtures and of the corresponding Ln^{3+} ion alone (Table 1, Figure F2, Supporting Information). The model used to fit the titration data was fairly complex, with six different $[Ln_iH_kL_j]^{(3i-4j+k)+}$ species: two hydroxide moieties (i = 1, j = 0, k = 1, 3), one unprotonated (k = 0) and two protonated 1:1 complexes (i = 1, j = 1, k = 1, 2), and one unprotonated 1:2 complex (i = 1, j = 2, k = 0). The speciation diagram for Eu is shown on Figure 2. In the case of La^{3+}, a spectrophotometric titration (Figure F3, Supporting Information) using a noncomplexing buffer ([Pipes] = 1.0×10^{-3} M)[37] was conducted at fixed pH = 7.00 ± 0.02, leading to two conditional stability constants: Log β_{110} = 7.3(2); Log β_{120} = 12.5(4). Transformation of these apparent stability constants into true constants by using the ligand pK_a's values and assuming the presence of nonprotonated complexes only resulted in a good agreement with potentiometric data. Ligand−metal stoichiometry used in the modeling of pH potentiometric data were suggested from spectrophotometric titrations and ESI-MS data on the Eu system. The podates are therefore quite stable, as demonstrated by the pLn values calculated with $[Ln]_t = 10^{-6}$ M, $[H_4L^1]_t = 10^{-5}$ M, and pH = 7.4: 9.3 for La, 10.0 for Eu, and 9.0 for Lu, as compared to 15.4 for $[Eu(edta)]^-$ [38] for instance. Monitoring the titration of L^1 with Ln^{3+} ions in D_2O (pD = 7) by ^{1}H NMR revealed that the largest chemical shift variations occur when

(34) Letkeman, P.; Martell, A. *Inorg. Chem.* **1979**, *18*, 1284.
(35) Barszcz, B.; Lenarcik, B. *Pol. J. Chem.* **1989**, *63*, 371.
(36) Linnell, R. H.; Kaczmarczyk, A. *J. Phys. Chem.* **1961**, *65*, 1196.
(37) Yu, Q.; Kandegedara, A.; Xu, Y.; Rorabacher, D. *Anal. Biochem.* **1997**, *253*, 50.
(38) Galaktionov, Y.; Astaklov, K. *Zh. Neorg. Khim.* **1963**, *8*, 460.

Table 2. Energy E of the $^1\pi\pi^*$ and $^3\pi\pi^*$ States and Lifetime (τ) of the $^3\pi\pi^*$ State of Ligand L^1 Alone or in the Ln 1:1 and 1:2 Podates, As Measured from Frozen Solutions in Ethanol (77 K)

		E/cm^{-1} [a]	
compound	τ /ms (2σ)	$^1\pi\pi^*$	$^3\pi\pi^*$
$[L^1]^{4-}$	0.10 (2)	33 715, 29 720	27 770, 27 095, ***26 295,*** 25 545, 24 865, 24 270, 23 450
$[LaL^1]^-$	0.128 (4)	33 610	25 865
$[La(L^1)_2]^{5-}$	0.104 (2)	33 610	25 865
$[GdL^1]^-$	0.45 (6)	33 645, 30 795, 28 985	27 625, 25 905, ***25 240,*** 24 650
$[Gd(L^1)_2]^{5-}$	0.15 (4)	33 645, 28 210	23 665
$[LuL^1]^-$	1.1 (4)	33 785, 30 635, 28 945	27 640, ***25 760,*** 25 070
$[Lu(L^1)_2]^{5-}$	0.44 (8)	33 785, 30 635, 28 390	24 020
$[EuL^1]^-$	0.50 (6)	33 510, 30 940, ***29 795***	24 840
$[Eu(L^1)_2]^{5-}$	0.71 (4)	33 510, 30 940, 28 555	25 445
$[TbL^1]^-$	0.63 (2)	33 510, 30 720, 27 880	b
$[Tb(L^1)_2]^{5-}$	0.84 (4)	33 510, 30 720, ***29 700***	b

[a] The most intense component is italicized. [b] Not detected due to $L^1 \rightarrow Tb^{3+}$ energy transfer.

the stoichiometry changes from 1:2 to 1:1, especially for benzyl and phenyl protons; this indicates that the metal ion is lying closer to the anchor in the 1:1 podates. The stability constants do not vary much from one Ln ion to the other. We have modeled $[GdL^1]^-$ in a vacuum with the program Cerius 2. The minimized structure points to π interactions between two neighboring pyrazole rings, which affect their orientation and consequently the binding of the N atoms to the metal ion. Single crystals of adequate quality could not be obtained for structural characterization.

Photophysical Properties of the Monomeric Podates. The photophysical properties of H_4L^1 and of its 1:1 and 1:2 monomeric podates with La, Eu, Gd, Tb, and Lu in dilute frozen ethanolic solutions (77 K) are summarized in Table 2 (see Figure F4, Supporting Information). UV excitation in the $\pi \rightarrow \pi^*$ and $n \rightarrow \pi^*$ absorption bands of the pyrazole units results in ligand-centered emission from L^1 displaying two structured and overlapping bands assigned to emission from the $^1\pi\pi^*$ and $^3\pi\pi^*$ states. The 0-phonon component of the singlet-state emission is located at 33 750 cm^{-1} while the corresponding transition from the triplet state occurs at 27 740 cm^{-1}. The overlap between the ligand $^1\pi\pi^*$ and $^3\pi\pi^*$ states induces an efficient intersystem crossing process. The $^3\pi\pi^*$ transition is not much altered in the 1:1 and 1:2 La podates, but complexation to Gd^{3+} and Lu^{3+} induces a broadening of the $^3\pi\pi^*$ emission band which has a relatively short (0.1 ms) lifetime. For the Eu and Tb podates, metal-centered emission is detected upon excitation in the $\pi \rightarrow \pi^*$ absorption band of the pyrazole units, but not when the samples are excited through the $n \rightarrow \pi^*$ state. As expected from the relatively high energy of the $^3\pi\pi^*$ 0-phonon component, Eu^{3+} is only weakly sensitized, particularly in the 1:1 podate, whereas good energy transfer occurs between the ligand $^3\pi\pi^*$ and $Tb(^5D_4)$ states. This is in agreement with what has been observed for Tb poly(aminocarboxylates) for which the more efficient antenna effect was observed for $^3\pi\pi^*$ states with energy around 26 000 cm^{-1} [39] and with the golden rule that the energy gap $\Delta E(^3\pi\pi^* - {}^5D_4)$ should be larger than 3500 cm^{-1} for efficient and irreversible energy transfer.[40]

The room-temperature emission spectrum of $(L^1)^{4-}$ in aqueous solution displays two bands centered at 26 350 and 23 050 cm^{-1} assigned as arising from the $^1n\pi^*$ and $^1\pi\pi^*$ states, respectively, which are progressively blue-shifted and the intensity of which decreases with increasing protonation of the ligand. No triplet-state emission is observed. Upon complexation, a 1000-cm^{-1} shift to lower energies occurs with increasing atomic number of the ion (Figure F5, Supporting Information). The luminescence intensity is pH dependent; for $[GdL^1]^-$ for instance, it goes through two maximums at pH 4 and 7. Ligand-centered luminescence quantum yields are reported in Table 3. They are respectively 2 and 3 times smaller in 1:2 and 1:1 podates compared to the value for the free ligand.

Table 3. Relative Quantum Yields (Q^{rel}). $[L^1]^{4-}$ (pH 13) and 1:1, 1:2 Complexes ($(0.5-1) \times 10^{-5}$ M) with Ln = La, Eu, Gd, Tb, and Lu in H_2O at pH 7

compound	Q^{rel}	λ_{exc}/nm	compound	Q^{rel}	λ_{exc}/nm
QSO_4	1	317	$[Lu(L^1)_2]^{5-}$	0.054	312
$[L^1]^{4-}$	0.11	317	$[Eu(terpy)_3]^{3+}$	1	437
$[LaL^1]^-$	0.029	317	$[Eu(L^1)]^-$	3.75	230
$[LaL^1_2]^{5-}$	0.046	317	$[Eu(L^1)_2]^{5-}$	0.50	230
$[GdL^1]^-$	0.019	317	$[Tb(terpy)_3]^{3+}$	1	409
$[Gd(L^1)_2]^{5-}$	0.041	317	$[TbL^1]^-$	1.04	230
$[LuL^1]^-$	0.035	312	$[Tb(L^1)_2]^{5-}$	0.62	230
				0.67	254

Metal-centered luminescence of dilute aqueous solutions is also pH dependent: 1:1 podates (Ln = Eu, Tb) display emission between pH 3 and 8.5, with maximum intensity occurring again at pH 4 and 7. In aqueous solution, Eu^{III} and Tb^{III} are equally sensitized, as shown by the absolute quantum yields of the 1:1 podates found to be equal to 4.9 and 5.0%, respectively. This points to a significantly improved energy transfer from the ligand to the $Eu(^5D_0)$ level in water over that found in frozen ethanol solutions (Figure F5, Supporting Information). We also note that the quantum yields of the 1:2 podates are about half the values found for the 1:1 complexes. Using the empirical equation proposed by Horrocks et al.[41] and the experimental lifetimes at room temperature for solutions of $[LnL^1]^-$ in H_2O (pH = 7.6) and D_2O (pD = 8.0), we determine the following average numbers of water molecules bonded in the inner coordination sphere of the metal ion: $q = 3.8 \pm 1.0$ and 4.9 ± 0.4 for the monomeric 1:1 podates with Eu and Tb, respectively.

Luminescence Enhancement of the 1:1 Monomeric Podates through Association With Cyclodextrins. Molecular modeling showed that partial inclusion of the 1:1 podates should occur in β-, βpm-, and γ-cyclodextrins. In the case of β-CD, ^1H NMR spectra of aqueous solutions demonstrate a deshielding of the aromatic anchor protons only, meaning that solely the anchor is included in the macrocyclic cavity. Moreover, the NMR data suggest a 1:1 association between the 1:1 podates and the cyclodextrin. Metal-centered emission increases considerably upon addition of CD, and the most spectacular luminescence enhancement is obtained with Tb (Figure F6, Supporting Information). Titrations conducted in both phosphorescence and fluorescence modes (Figure 3 and Figure F6, Supporting Information) allowed us to estimate the apparent association constants of the Tb 1:1 podate with CDs in the following way.

The metal-centered phosphorescence intensity of $[TbL^1]^-$ without CD can be written as

$$I_0(\lambda) = C_{10}{}^0[TbL^1]$$

where $C_{10}{}^0$ is a constant that incorporates the quantum yield and the absorptivity of the complex in the absence of CD. In the presence of CD, the formation of a host−guest adduct leads

(39) Latva, M.; Takalo, H.; Mukkala, V. M.; Matachescu, C.; Rodriguez-Ubis, J. C.; Kankare, J. *J. Lumin.* **1997**, *75*, 149.

(40) Steemers, F. J.; Verboom, W.; Reinhoudt, D. N.; van der Tool, E. B.; Verhoeven, J. W. *J. Am. Chem. Soc.* **1995**, *117*, 9408.

(41) Horrocks, W.; De, W., Jr.; Sudnick, D. R., Jr. *J. Am. Chem. Soc.* **1979**, *101*, 334.

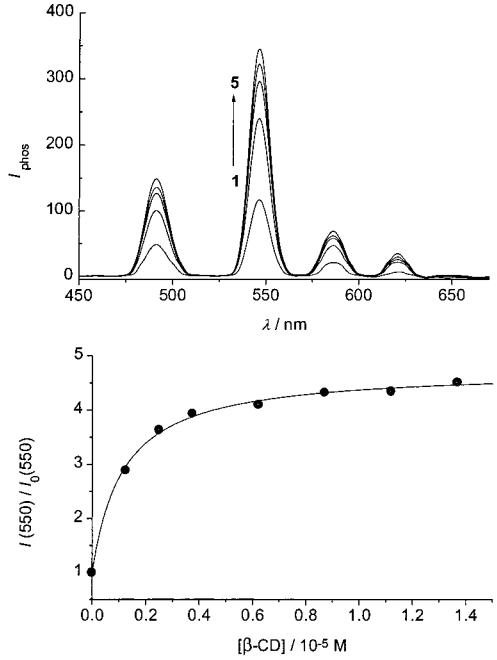

Figure 3. Titration of $[TbL^1]^-$ 5×10^{-6} M in H_2O by β-CD. Top: emission spectra at [β-CD] = (0, 1.2, 2.5, 6.2, and 8.7) $\times 10^{-6}$ M. Bottom: increase of the phosphorescence intensity at 550 nm vs [β-CD]. $\lambda_{exc} = 260$ nm; pH = 7.30 ± 0.03.

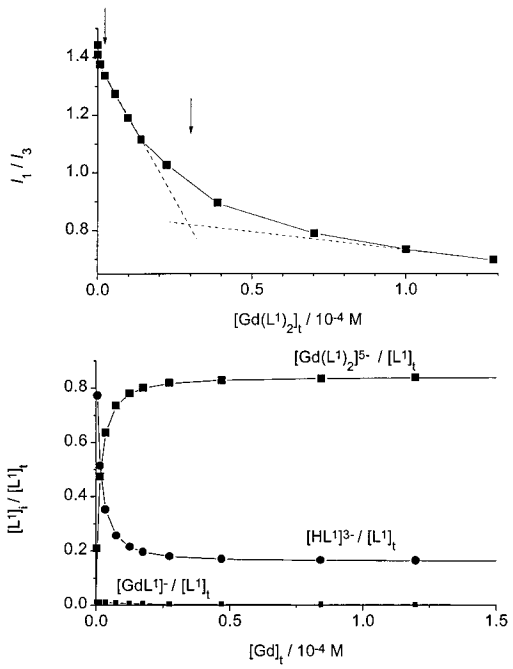

Figure 4. Top: I_1/I_3 ratio of pyrene fluorescence vs $[Gd(L^1)_2]^{5-}$ computed concentration (arrows point to the observed breaks). Bottom: computed distributions of the various L^1 species, pH = 9.2.

Table 4. Association Constants (K_{11}) for 1:1 Complexes between $[L^1Tb]^-$ and CDs and Phosphorescence Enhancement Ratio (C_{11}/C^0_{10}) Obtained from Luminescence Titrations. $[L^1]_t = [TbCl_3]_t = 5 \times 10^{-6}$ M; pH 7.30 ± 0.03; $T = 20.0$ °C

host	Log K_{11} (±2σ)	C_{11}/C^0_{10}
β-CD	6.0 (2)	4.2 (4)
βpm-CD	5.1 (2)	4.2 (2)
γ-CD	5.3 (1)	2.7 (1)

to a global phosphorescence intensity $I(\lambda)$ at a given wavelength:

$$I(\lambda) = C_{10}[TbL^1] + C_{11}[TbL^1 \subset CD]$$

For each titration, we were able to show that $C_{10}^0 = C_{10}$, so that combining the previous expressions leads to

$$I(\lambda)/I_0(\lambda) = \frac{1 + (C_{11}/C_{10}^0)K_{11}[CD]}{1 + K_{11}[CD]}, \quad \text{with}$$

$$K_{11} = \frac{[TbL^1 \subset CD]}{[TbL^1][CD]}$$

The association constants K_{11} and the phosphorescence enhancement ratios (C_{11}/C_{10}) upon CD complexation were introduced as fitting parameters in the nonlinear regression of the experimental $I(\lambda)/I_0(\lambda)$ values as a function of CD concentration. The binding constants reported in Table 4 are ~3 orders of magnitude larger compared to association constants between β-CD and transition metal complexes with macrocycles[42] or cyclopentadienyl ligands.[43] The magnitude of K_{11} increases with the hydrophobic character of CDs, meaning that hydrophobic interactions and the concomitant release of solvent molecules represent important favorable factors in the driving force leading to the association. We note indeed that the phosphorescence enhancement ratio C_{11}/C_{10} decreases with the polarity of the CD; e.g., β-CD < γ-CD.

Self-Aggregation of the 1:2 Podates. As expected from the design of the encapsulating podand, turbidity due to self-aggregation appears at relatively low concentration, ~10^{-4} M. The aggregation behavior of the $[La(L^1)_2]^{5-}$ podate was investigated by ^1H NMR spectroscopy in D_2O at pD = 7.5. All the protons become shielded upon increasing the concentration (Figure F7 Supporting Information), the largest chemical shifts being obtained for the benzene protons, which can be attributed to an intermolecular aromatic ring current taking place in the aggregates.[44] The shielding of the benzene protons as the concentration increases points to a stacking between hydrophobic anchors contributing to the aggregation process. We believe that the formation of self-aggregates originates from weak intermolecular interactions and not from strong metal−ligand bonds inducing polymerization, mainly because the stacking interaction observed between phenylene anchors would not be possible in a polymeric network. Moreover, no oligomers were detected by ESI-MS in methanolic solutions of the Eu podates. On the other hand, the smaller chemical shift experienced by the pyrazole protons means that these moieties participate less than expected in the association process.

The aggregates were characterized by three different experimental techniques. First, the intensity ratio between the first and third vibrational components of the pyrene fluorescence band at 363 and 382 nm, I_1/I_3, was used as polarity probe.[45] Upon addition of $[Gd(L^1)_2]^{5-}$ to pyrene-saturated water, two breaks are observed in the I_1/I_3 ratio at $[Gd(L^1)_2]^{5-} = (8.0 \pm 0.3) \times 10^{-7}$ and $(3.2 \pm 0.2) \times 10^{-5}$ M (Figure 4). The first one reflects the rise in the concentration of the 1:2 species as shown by the speciation curves computed from the stability constants. The second break points to the beginning of the aggregation process. Opalescence of the solution starts at ~9×10^{-5} M and reflects the formation of higher aggregates.

(42) Raj, C. R.; Ramaraj, R. *Electrochemica Acta* **1999**, *44*, 2685.
(43) Wang, Y.; Mendoza, S.; Kaifer, A. E. *Inorg. Chem.* **1998**, *37*, 317.
(44) Haigh, C. W.; Mallion, R. B. *Prog. Nucl. Magn. Reson. Spectrosc.* **1980**, *13*, 303.
(45) Winnik, F. M. Regismond, S. T. A. *Colloid Surf. A: Physicochem. Eng. Aspects* **1996**, *118*, 1.

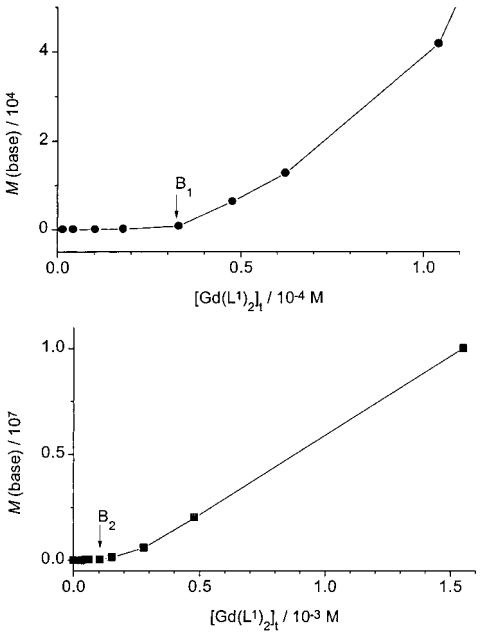

Figure 5. Plots of the correlation curve baseline values as a function of $[Gd(L^1)_2]^{5-}$, at 22 °C, pH 9.2 for the determination of critical aggregation concentrations. Top: first part of the curve. Bottom: entire curve.

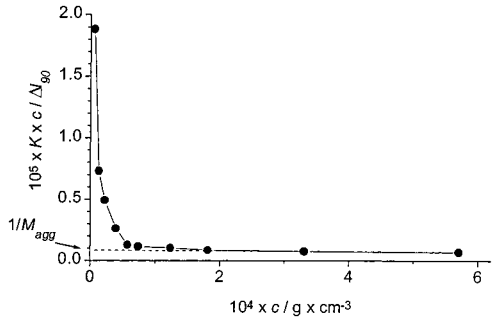

Figure 6. Determination of the average mass of the $\{[Gd(L^1)_2]^{5-}\}_n$ aggregates (M_{agg}) in H_2O at pH 9.2, using a plot of $Kc/\Delta I_{90}$ (see text) vs the monomer molality c.

Second, the critical aggregation concentrations were determined by measuring the concentration dependence of the light-scattering ratio $I^{sol}/I^{toluene}$. A plot of the correlation curve baseline value, M(base), computed from these data (Figure 5) presents two discontinuities at 3.5×10^{-5} M (cac-1), in good agreement with fluorescence measurements, and at 10^{-4} M (cac-2). The presence of a second cac indicates a change in the nucleation process of monomeric $[Gd(L^1)_2]^{5-}$. Analysis of the correlation curves reveals the presence of three types of particles with the following mean hydrodynamic radii: (i) 11 ± 1 nm, which account for all the diffusion in the concentration range between cac-1 and cac-2, (ii) 57 ± 15 nm, which become the major particles in solution at concentrations larger than cac-2, and (iii) 280 ± 80 nm corresponding to the coagulation of the previous particles; the proportion of these large particles increases with increasing concentration until 5×10^{-4} M, where they are the more numerous particles in solution and stay constant up to 1.55×10^{-3} M, the highest concentration investigated.

The average aggregation number N_{agg} of the 1:2 podates was estimated from a plot of $Kc/\Delta I_{90}$ as a function of the solute concentration c (Figure 6). In this expression, K is defined as follows for the vertically polarized incident light:[46]

$$K = 4\pi^2 n_0^2 (dn/dc)^2 / N_A \lambda^4$$

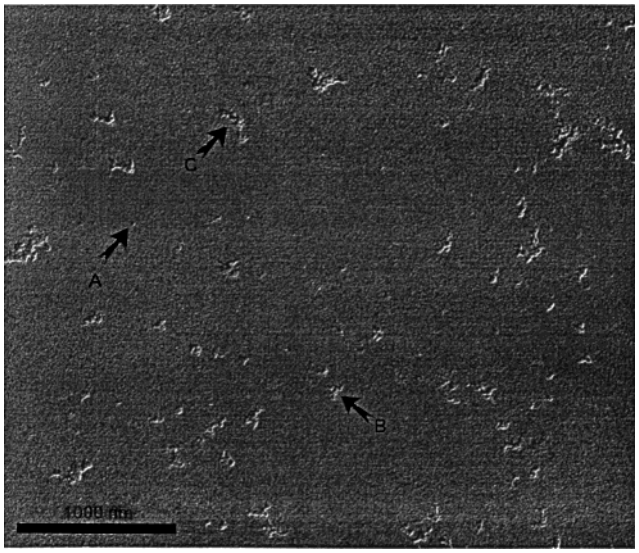

Figure 7. Pseudo-3D transmission electron micrograph of the $\{[Gd(L^1)_2]^{5-}\}_n$ particles and aggregates collected on the Au grid after deposition of 2 μL of the 1.1×10^{-4} M solution on a gold grid and washing with a drop of pure water. The pseudo-3D effect was obtained by applying an asymmetric 3×3 matrix filter emphasizing the topographic contrast of the original negative. The arrows point to typical classes of particles: 20−30 (A), 70−90 (B), and >100 nm (C).

where n_0 and n stand for the refractive indices of the solvent and the solution, respectively, N_A is the Avogadro number, λ is the wavelength of the incident light, and ΔI_{90} is the Rayleigh diffusion ratio of the solution in excess to that of a solution with a concentration equal to cac-1; dn/dc was calculated from refractive index measurements and found to be 0.39. Extrapolation of the curve to $c = 0$ yields the inverse of the aggregate molecular weight M_{agg} from which the average aggregation number N_{agg} can be estimated. In the case of $[Gd(L)_2]^{5-}$, this number corresponds to ~1050 monomers ($M_{agg} \approx 1.8 \times 10^6$ g·mol^{-1}).

Finally, information on the shape and size of the aggregated particles was obtained from transmission electron microscopy of centrifuged or deposited particles. The particles revealed to be spherical (Figure 7 and Figure F8, Supporting Information) and two mean diameters could be directly determined by this technique, 20 and 60 nm. The particles are amorphous, as revealed by diffraction experiments, and they have a large electron density reflecting a high gadolinium content but are potassium free, as shown by energy dispersive spectroscopy (Figure 8 and Figure F9, Supporting Information). The very similar elemental composition of the two kinds of spherical particles can probably be traced back to a second nucleation phenomenon leading to larger aggregates from the 20-nm ones. There are also a few much larger aggregates with a size of ~300 nm, similar to those observed in solution. Counting the particles lying on a 14-μm^2 surface, after deposition of a 1.2×10^{-4} M solution of $[Gd(L^1)_2]^{5-}$ on a gold grid and evaporation of the solvent, led to the following statistics: 68% of 15−45-nm particles, 25% of 60-nm particles, and 7% of larger particles. Smaller aggregates could not be accurately discriminated from their background (collodion−carbon film) under our experimental conditions, although light-scattering measurements indicate the presence of 10-nm entities. The larger share of the bigger particles can be explained by the experimental conditions favoring their deposition and making them more resistant to washing of the grid with water.

(46) Taboada, P.; Attwood, D.; Ruso, J. M.; Sarmiento, F.; Mosquera, V. *Langmuir* **1999**, *15*, 2022.

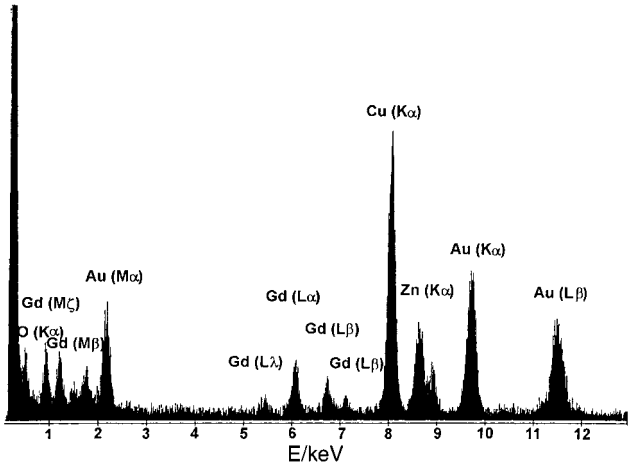

Figure 8. Energy dispersion spectrum of 20-nm spherical particles of $\{[Gd(L^1)_2]^{5-}\}$. The Au signal originates from the gold supporting grid. Cu and Zn signals originate from pieces of the microscope.

Statistical fractal analysis of the deposited larger self-aggregates was used to determine the main kinetic regime of their formation from the smaller particles. The kinetics of colloid aggregation is related to the structure and morphology of the particles and clusters formed.[31,47,48] Namely, the mass m_{agg} or volume V_{agg} of the aggregates can be described in function of their morphological features:

$$m_{agg} \propto V_{agg} \propto ((R_g)_{agg}/(a)_{unit})^f$$

with the exponent f representing the fractal dimension of the aggregates, i.e., the self-similarity of their structure.[31] When elementary colloids with radius $(a)_{unit}$ collide to produce an aggregate with a radius of gyration $(R_g)_{agg}$, their aggregation rate may be controlled either by Brownian motion (diffusion-limited colloid aggregation, DLCA) or by electrostatic repulsive forces (reaction-limited colloid aggregation, RLCA). The DLCA mechanism is induced by attractive van der Waals forces and is usually an irreversible process, while RLCA requires that elementary colloids overcome their repulsive barrier to stay in close contact. The fractal dimension allows one to differentiate between these two regimes: $f \approx 1.8$ for DCLA and $f \approx 2.1$ for RLCA. While the aggregates can be analyzed by light-scattering techniques at a bulk level, electron microscopy provides an insight into the characteristics of the individual entities. Figure 9 shows the results of the fractal analysis performed on TEM images of individual self-aggregates. A Log−Log plot of the equation above yields $f = 2.21(4)$, which is in good agreement with values reported for reaction-limited colloid aggregation.[32,48] The radius of the elementary particles within the aggregates was taken as $(a)_{unit} = 8.25$ nm ($Ø_{unit} = 16.5$ nm). The fractal dimension was checked to be insensitive to the size of the elementary particles for $(a)_{unit} = 5$ (light scattering), 8.25 (TEM), and 15 nm (arbitrary size). Moreover, to test the statistical relevance of the calculated fractal dimension of our system, a fit was enforced with $f = 1.8$ (representative of DLCA), but this slope produced a significantly larger χ^2 value. Finally, fits under boundary limits taking into account the propagation of experimental errors on $(V_{calc})_{agg}$ and $(R_g)_{agg}$ yielded fractal dimensions comprised between 2.13(4) ($V_{max} \propto (R_g/a)^{f_{min}}$) and 2.34(6) ($V_{min} \propto (R_g/a)^{f_{max}}$), which defines the variability range of the actual f value. The reaction-limited aggregation of the

(47) *Aggregation and Fractal Aggregates*; Jullien, R., Botet, R., Eds.; World Scientific: Singapore, 1987.

(48) Julien, R. *New J. Chem.* **1990**, *14*, 239.

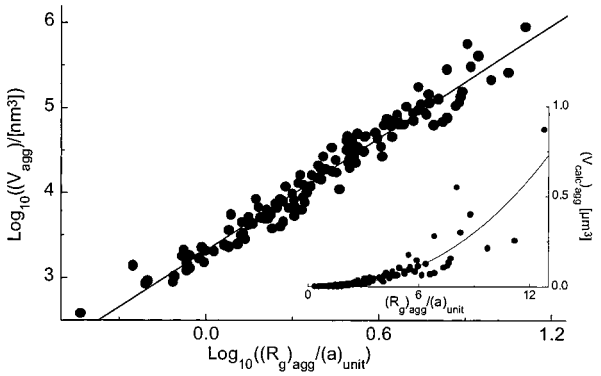

Figure 9. Plot of the volume of $\{[Gd(L^1)_2]^{5-}\}_n$ particles and aggregates vs the ratio (radius of gyration of aggregate)/(radius of their elementary units), as determined by image analysis on electron micrographs (128 entities). The inset shows the raw data; the power-law fitting was calculated on the Log−Log representation to minimize the statistical weight of the large $(R_g)_{agg}/(a)_{unit}$ on the results.

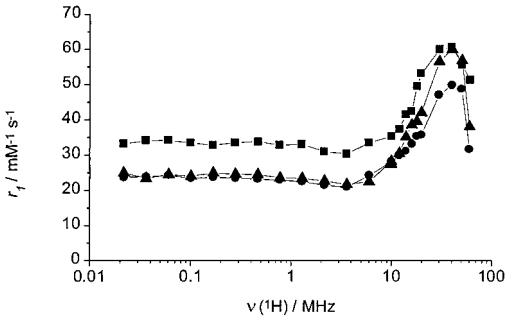

Figure 10. NMRD profiles of $\{[GdL^1_2]\}_n^{n5-}$ at 5 (▲), 25 (■), and 75 °C (●); pH 7.2 (pipes).

$\{Gd(L^1)_2{}^{5-}\}_n$ entities can be explained in terms of the structure of the constitutive podates, which is highly charged while bearing a hydrophobic moiety, the aromatic anchor. Stacking of the podates via their anchor, as suggested by the NMR shifts, allows the formed entities to minimize their electrostatic repulsion and the total entropy of the growing self-aggregates. The ill-defined morphology of the aggregates analyzed by TEM confirms the absence of crystallinity of the species and suggests that stacking must proceed by an isotropic scheme.

The formation of spherical $\{Gd(L^1)_2{}^{5-}\}_n$ self-aggregates with 10-nm diameter and their subsequent coagulation into larger structures suggests that the particles are perhaps less negatively charged than the formal $-5n$ value, because electric repulsion could otherwise be larger than the forces responsible for coagulation. In an effort to estimate the effective charge of the particles, we have measured their electrophoretic mobility μ_e and extracted the ζ potential. The resulting ζ curves obtained for $\{Gd(L^1)_2\}^{5n-}$ particles in water at pH 7.4 display a peak, centered at -31.9 (5) mV, indicating negatively charged aggregates and good colloidal stabilization because of electric repulsion. The surface charge density (σ_0) was evaluated to be 6.14×10^{-3} C/m^2. This estimation is 10−20 times smaller than expected. Charge compensation therefore occurs, which could be due to the presence of cations such as H_3O^+ or K^+ in the mother liquor during the synthesis. This is supported by the microanalyses which effectively indicate the presence of these counterions (see Experimental Section).

Water Proton Relaxation of the Self-Aggregated 1:2 Gd Podate. The proton relaxivity of a solution of Gd 1:2 podate is reported on Figure 10. The high-field peak in the range 20−60 MHz is an indication of a slow rotational correlation time and of a high rigidity of the system. This can only be explained by

Table 5. Relaxivity of the Most Interesting Gadolinium-Containing Contrast Agents for MRI Compared to That of the L^1 Podates

ligand	r_1 per Gd/mM^{-1} s^{-1}	conditions
DTPA	4.3[a]	25 °C; 20 MHz
DTPA−BMA	4.39[a]	25 °C; 20 MHz
DOTA	4.2[a]	25 °C; 20 MHz
linear polymers	6−18[a]	37 °C; 20 MHz
dendrimeric compounds	11−36[a]	37 °C; 20 MHz
natural polymer-based macromolecular agents covalent conjugates	7−14[a]	37 °C; 10/20 MHz
noncovalent protein adducts	up to 40−50[a,b]	37 °C; 20 MHz 4.5% HAS
$\{[Gd(L^1)_2]\}_n^{5-n}$	53	25 °C; 20 MHz
$\{[GdL^1]\}_n^{n-}$	18[c]	25 °C; 20 MHz

[a] From ref 2. [b] Observed values in 4.5% HSA. [c] Observed value. The relaxivity has been determined in a solution that initially contained 87.5% $[GdL^1]^-$ and 12.5% $[Gd(L^1)_2]^{5-}$ according to the speciation. The computed relaxivity for pure $\{[GdL^1]\}_n^{n-}$ amounts to $r_1 = 13$ $mM^{-1}s^{-1}$.

the presence of nanometric particles in solution obtained through monomer aggregation, as demonstrated above. Proton relaxivity measured at 10 MHz slightly decreases (5−10%) upon decreasing the $[Gd(L^1)_2]^{5-}$ concentration from 1.5×10^{-3} to 1.5×10^{-4} M, suggesting that the particle size is somewhat affected by concentration changes, as pointed out by light-scattering measurements. Characteristic peaks in longitudinal proton relaxivity profiles have been observed for superparamagnetic species.[49] However, this possibility can be excluded in the present case since the Gd^{III} ions in these nanometric particles are located too far from each other to generate magnetic interactions leading to superparamagnetic effect. Furthermore, the relaxivity peaks found for superparamagnetic systems are usually much broader and their maximum is rather at lower frequencies (around 10 MHz). Consequently, the only explanation for the presence of the high-field peak in the NMRD profiles of the Gd podate is the slow rotation of the aggregates.

The astounding result is that solutions of the 1:2 Gd podate display a very large relaxivity, which amounts to $r_1 = 53$ mM^{-1} s^{-1} at 25° C and 20 MHz; that is 12.6 times larger than the widely used $[Gd(DOTA)]^-$ contrast agent and larger than the relaxivity of adducts between contrast agents and proteins[2] (Table 5). In the case of contrast agents obtained from noncovalent association between proteins and Gd chelates, the measured values of the water relaxivity are not higher than 40−50 mM^{-1} s^{-1} and the association constants of the adducts are not always very high; thus the adducts are not fully formed. This means that the measured relaxivity is lower than the calculated bound relaxivity. Moreover, because of the high molecular weight of these proteins, the measured relaxivity of millimolar solutions of the Gd complexes is often overestimated by up to 25% because their molality is in fact larger.[5] Interest in larger particles with contrast agent ability, such as those generated in $\{Gd(L^1)_2\}_n^{5n-}$ solutions, stems from their large retention time in blood, a prerequisite for angiographic applications. Another advantage of $\{Gd(L^1)_2\}_n^{5n-}$ over the existing contrast agent systems lies in the fact that the rigid, but porous, nanometric particles it generates display at 25 °C a large and almost constant relaxivity in the frequency range 30−50 MHz, which is important for biomedical applications. Many of the known supramolecular systems have a sharper relaxivity peak around 20 MHz followed by an abrupt drop at higher frequencies. We also note that the NMRD profiles are temperature dependent, while displaying always a high relaxivity (Figure 10), pointing to aggregation being temperature dependent. Finally, to test the potentiality of the described system to be used in in vivo analyses,[50] we have added an equimolar quantity of Zn^{II} (with respect to Gd^{III}) and found that after 1 day the relaxivity remains unchanged, meaning that the transition metal ions does not replace Gd^{III} inside the self-aggregated particles.

Proton relaxivity is determined by numerous parameters, involving correlation times for rotation, water exchange and electronic relaxation, the number of inner-sphere water molecules, the ^1H-Gd distance (inner-sphere relaxation term), and the diffusion correlation time (outer-sphere relaxation term). The transverse electron spin relaxation rate of the $\{Gd(L^1)_2\}_n^{5n-}$ system has been estimated from X-band EPR measurements to be around 9×10^9 s^{-1} ($B = 0.34$ T). Unfortunately, due to solubility problems, ^{17}O NMR measurements could not be performed to determined the water exchange rate. Furthermore, $\{Gd(L^1)_2\}_n^{5n-}$ self-aggregates are quite complex with differently sized nanometric particles. As a consequence, reliable fits of the NMRD profiles could not be generated. The lower relaxivity obtained for the $\{GdL^1\}_n^{n-}$ aggregates (Table 5) can be explained partially from the TEM experiments on deposited aggregates on gold grids which reveal that the size of the particles is smaller than 130 nm in any case, most of them being in the 20−40-nm range.

Conclusion

We have synthesized a predisposed podand H_4L^1 able to encapsulate trivalent lanthanide ions and to generate secondary supramolecular structures through hydrophobic and weak multiple interactions. The resulting 1:1 and 1:2 lanthanide podates display a good stability under physiological conditions with, for instance, a computed pEu = 10. Investigations of photophysical properties of the lanthanide complexes reveal that pyrazole units provide a relatively efficient energy transfer to $Eu(^5D_0)$ and $Tb(^5D_4)$ excited states and act therefore as good energy harvesters; a quantum yield of 5% is obtained in the case of the $[TbL^1]^-$. Addition of β-CD to solutions of the 1:1 podates leads to strong association and to a more than a 4-fold increase in the metal-centered luminescence (quantum yield ~20%). Due to the flexible design of the podand H_4L^1, improvement of its antenna effect shifting the $^3\pi\pi^*$ state to somewhat lower energy and by increasing the molar absorbance of the podand appears to be within reach, for instance by adding a chromophoric residue on the 5-position of the pyrazole units.

Secondary supramolecular interactions occur in solution and the $[Ln(L^1)_2]^{5-}$ podates aggregate into spherical, rigid, but porous nanoparticles of low dispersivity, with 10- and 60-nm diameter, which further coagulate into nonsymmetrical larger structures (~280−300 nm). Generation of aggregates at $\sim 10^{-3}$ M is a fast process ($t_{1/2}$ in the range of seconds at 20 °C), and colloidal solutions are stable over weeks at room temperature, without showing sedimentation. Nanosized spherical particles are obtained instead of microcrystals because in the conditions used the growth of the nanometric supramolecular edifices is too fast to generate a regular stacking between hydrophobic surfaces. Fractal analysis of TEM-generated images of the particles points to a pure reaction-limited regime generating the larger self-aggregates under the experimental conditions used. This regime occurs when the repulsive forces between the particles are the limiting factor, inducing the formation of compact aggregates, reasonably rigid although porous. It is

(49) Bulte, J. W. M.; Brooks, R. A.; Moskowitz, B. M.; Bryant, L. H.; Frank, J. A. *Magn. Reson. Med.* **1999**, *42*, 379.

(50) Bünzli, J.-C. G.; Fatin-Rouge, N. United States Provisional Patent Application USSN 60/170,311, Dec 13, 1999.

known that other kinetic regimes of aggregation can be obtained by changing the experimental conditions (ionic strength, concentration, temperature), which opens the way for the design of size-controlled nanoparticles with enhanced physicochemical properties.

The porous supramolecular structure of the self-aggregates allows free circulation of water inside the edifice, which explains why solutions of the Gd 1:2 podate display the largest relaxivity ever reported for a gadolinium chelate, more than 1 order of magnitude larger than the relaxivity of the first-generation contrast agents. Two problems associated with the supermolecules designed as MRI contrast agents[9,10] are the presence of internal motions reducing their rigidity and leading to a lower relaxivity than expected and the large amount of nondirectly active substance needed for a MRI measurement. The system described here avoids both disadvantages and points to potential applications in various fields of medical diagnosis, including angyology and in vivo temperature mapping. Several clues show that control of the coagulation process of the spherical particles, that is, of their molecular mass, size, and shape, is possible,[32] which leads us to foresee further improvement in the properties of these systems, for instance with respect to the ability to control their relaxivity reversibly, depending on the size and number of the nanoparticles in solution. In conclusion, the new supramolecular methodology we are developing to synthesize both contrast agents for MRI and luminescent stains for medical analysis or for the luminescent mapping of biomolecules seems to be quite promising.

Acknowledgment. We thank Dr P. Bowen for helpful discussion on the aggregation processes. This research is supported through grants by the Swiss National Science Foundation. A.E.M. thanks the Swiss Federal Office for Education and Research for a grant (COST Action D8) and J.-C.G. B. thanks the Fondation Herbette (Lausanne) for the gift of spectroscopic equipment.

Supporting Information Available: Figures showing the spectrophotometric titration of $[L^1]^{4-}$ with H_3O^+ and of $[HL^1]^{3-}$ by La^{3+}, and the potentiometric titration of H_4L^1 and (H_4L^1 + Eu) with KOH. Figures displaying the low-resolution and time-resolved spectra of the ligand-centered and metal-centered luminescence in frozen ethanol and water, figure showing the influence on the Tb-luminescence of β-CD addition to aqueous $[TbL^1]^-$ solution, figure displaying the variation of the ^{1}H NMR shifts upon concentration of $[La(L^1)_2]^{5-}$, transmission electron micrographs of $\{[Gd(L^1)_2]^{5-}\}_n$ particles, energy disperson spectrum of 60-nm spherical particles of $\{[Gd(L^1)_2]^{5-}\}_n$ (PDF). This material is available free of charge via the Internet at http://pubs.acs.org.

JA001089B